Structure, microstructure, and high-temperature transport properties of $La_{1-x}Ca_xMnO_{3-\delta}$ thin films and polycrystalline bulk materials

M. H. Aguirre,[1,a)] S. Canulescu,[2] R. Robert,[1] N. Homazava,[1] D. Logvinovich,[1] L. Bocher,[1] Th. Lippert,[2] M. Döbeli,[3] and A. Weidenkaff[1]
[1]*Empa, Solid State Chemistry and Catalysis, CH-8600, Dübendorf, Switzerland*
[2]*Paul Scherrer Institut, General Energy Research Department, CH-5232, Villigen, Switzerland*
[3]*Ion Beam Physics, Paul Scherrer Institut c/o ETH, CH-8093, Zürich, Switzerland*

(Received 11 October 2007; accepted 9 November 2007; published online 11 January 2008)

Single-phase samples of $La_{1-x}Ca_xMnO_{3-\delta}$ (LCMO), $x \approx 0.3$, prepared by pulsed reactive crossed beam laser ablation on $SrTiO_3$ (STO) substrates, and soft chemistry synthesized powders were studied by various methods. The precise study of the crystal structure and microstructures by a combination of electron diffraction and high-resolution electron microscopy revealed a monoclinic distortion of the $GdFeO_3$-type structure, $P2_1/c$ space group, in both types of materials, i.e., the thin films and powder compound. The analysis of the LCMO/STO interface showed nonhomogeneous stress states and a composition that results in a different superstructure from the usual detected structure. The temperature-dependent thermoelectric power in the case of thin films presented an anomalous behavior compared to those from the powder compound. A structural transition at high temperature ($T \approx 750$ K) influences the thermopower behavior as well as the thermal conductivity values. © *2008 American Institute of Physics*. [DOI: 10.1063/1.2826950]

I. INTRODUCTION

The complex interplay between the structure, magnetic, and transport properties of $A_{1-x}A'_xMnO_3$ perovskite materials (with A^{3+}, a rare earth, and A'^{2+}=Ca, Sr, Ba, etc.) has generated much interest, since this is the starting point to understanding colossal magnetoresistance (CMR). The origin of the CMR effect is so far not elucidated, even though the influence of the A and A' sizes has been studied.[1] It is generally agreed that the creation of mixed-valence states, where both Mn^{3+} and Mn^{4+} ions are present, is essential for the double-exchange interaction.[2] The family of $La_{1-x}Ca_xMnO_3$ is particularly interesting since it can be prepared over the whole range of doping. The parent compound $LaMnO_3$ (Mn^{3+}, i.e., $t_{2g}^3e_g^1$) is an antiferromagnetic insulator. The substitution on the La^{3+} site by a divalent alkaline earth ion results in a mixed valence of the Mn^{3+}/Mn^{4+} states, where the Mn^{4+} ionic state has no e_g electron ($t_{2g}^3e_g^0$). The itinerant hole associated with the Mn^{4+} ion may hop to the Mn^{3+} sites, but the hopping is only favored to sites with parallel localized spins.[3] In general, the hole carrier density and the overlap between the manganese and oxygen orbitals are two key parameters that govern the transport properties of the system. The transport properties are closely related to the modification of the MnO_6 octahedron with a direct influence on the Mn–O–Mn angles. Usually, $La_{1-x}Ca_xMnO_3$ is reported as orthorhombic, i.e., distorted from the cubic perovskite structure ($a_p\sqrt{2} \times 2a_p \times a_p\sqrt{2}$, with $a_p \approx 0.4$ nm parameter of cubic perovskite). Due to the pseudocubic symmetry, this material presents microdomains, twinning, and defects that eventually do not allow detection of a tiny distortion of the unit cell when the material is studied by x-ray or neutron diffraction.[4] Moreover, the metal-insulator transition property, especially in thin films, is extremely sensitive to hydrostatic pressure, mismatch epitaxy stress, and the "chemical pressure" described by the tolerance factor.[1,5,6]

In this work, a detailed transmission electron microscopy study (TEM) by high-resolution electron imaging (HREM) and electron diffraction (SAED) for the $La_{1-x}Ca_xMnO_{3-\delta}$ (LCMO) powder compound and thin film growth on $SrTiO_3$ (STO), with $x \approx 0.3$, are reported. The Seebeck coefficient, resistivity, and thermal conductivity in a broad range of temperatures were measured for both materials. The objective is to obtain important information about the electronic nature of the carrier type and relate them to the structural changes and transitions.

II. EXPERIMENTAL

LCMO films on single-crystal STO (100) substrates were obtained by a variation of pulsed laser deposition (PLD), i.e., pulsed reactive crossed-beam laser ablation (PRCLA), with thicknesses ranging from 200 to 250 nm. The source was a sintered target with a composition $La_{0.6}Ca_{0.4}MnO_3$, which has been confirmed by laser ablation inductively coupled plasma–atomic emission spectrometry. More details about the PRCLA method can be found elsewhere.[7–9] Fine powders with a similar composition were prepared by soft chemistry from La_2O_3 (Alfa Aesar, 99.99%, fired at 800 °C prior to use), $CaCO_3$ (Aldrich, 99+%), and $Mn(NO_3)_2$ (Aldrich, 49.7 wt. % solution in dilute nitric acid). The formation of the perovskite phases from water soluble precursors is described elsewhere.[10,11] The soft chemistry method allows production of polycrystalline materials, avoiding possible inhomogeneous cationic distribution, and where the synthesis temperature is reduced, preventing anion vacancy formations.

a)Electronic mail: myriam.aguirre@empa.ch.

X-ray diffraction patterns of thin films, to check the epitaxial relationship between the substrate and thin film, were recorded by a Siemens D5000 diffractometer using monochromatic $K\alpha_1$ radiation ($\lambda = 1.54056$ Å), and equipped with an Eulerian cradle. The powder sample was measured by x-ray diffraction using a Philips X'Pert PRO MPD Θ-Θ system equipped with a linear detector (X'Celerator).

Thin films on substrates were thinned in cross-sectional geometry by two different methods, i.e., the tripod method, and by a dimple grinder (Gatan model 656). The final electron transparency was achieved by an ion-beam milling system (RES 101 from Baltec). For powder samples, TEM was performed using Cu grids on which the powder-alcohol suspension was deposited. Low- and high-resolution TEM and SAED were performed on a Philips CM30 microscope equipped with an energy-dispersive x-ray detector (EDAX model) to perform energy-dispersive x-ray spectroscopy (EDX) for the elemental composition. In the case of thin films, the composition was also confirmed by Rutherford backscattering (RBS) and elastic recoil detection analysis (ERDA) under the experimental conditions described in Ref. 9.

The thermal conductivity, κ, of the sintered disk-shaped pellets was determined from their density, d, thermal diffusivity, α, and specific heat, c_p, using the relationship $\kappa = d^* \alpha^* c_p$. The thermal diffusivity was measured using a Netzsch LFA 457 laser flash analyzer in the temperature range of 300–1273 K under argon atmosphere. The specific heat, c_p, was measured using a NETZSCH model DSC 404 C Pegasus differential scanning calorimeter under synthetic air atmosphere.

The electrical transport property measurements were done on a sintered bar-shaped pellet from the powder, and on the thin-film/substrate samples. The electrical conductivity and the Seebeck coefficient were measured in the temperature range from 340 to 1240 K in air using the RZ2001i measurement system from Ozawa Science, Japan. The Seebeck coefficient was measured by the steady-state method, and the electrical conductivity was measured by the dc four-probe method. Two electrical contacts were placed at the ends of the sample and the other two on the sample body. The contacts at the ends were made mechanically with Pt layers. The contacts on the pellet body were made by surrounding the bar-shaped sample with Pt wires, in the case of powder-sintered samples, while extra Pt paste was added on the film/substrate.

The oxygen content was determined by the hot gas-extraction (HGE) method using a LECO TC500 analyzer. A small aliquot of the sample (roughly 15 mg) was placed in a graphite crucible, which was heated to 3273 K within a few seconds using an inductive furnace. At that temperature lattice oxygen reacts with carbon from the crucible to form CO. The amount of CO was determined using an infrared detector. Silicon oxide was used as a calibration standard for oxygen.

The oxidation state of Mn in $La_{1-x}Ca_xMnO_3$ was determined by redox titration with potassium permanganate.[12] 25 mg of the powder was dissolved in 20.0 mL of 0.05 M ferrous ammonium sulfate acidified solution (2% H_2SO_4 v/v).

TABLE I. Compositional studies of powder and thin-film samples by EDX and RBS/ERDA measurements.

		Thin film		
	Powder sample	EDX		RBS
Element	EDX	Near surface	Near interface	($\Delta \approx 6\%$)
La	0.630±0.050	0.690±0.050	0.770±0.050	0.740
Ca	0.3650±0.040	0.315±0.040	0.235±0.040	0.280
Mn	0.950±0.050	0.895±0.010	0.800±0.010	1.000
O	2.950±0.050 (HGE: 2.90±0.05)	2.800±0.150	2.700±0.150	2.770 (ERDA)

During dissolution the powder reacts with ferrous ammonium sulfate solution, oxidizing the Fe^{2+} to Fe^{3+}, whereas Mn^{3+} and Mn^{4+} are reduced to Mn^{2+} according to the reaction

$$Mn^{y+} + (y-2)Fe^{2+} \rightarrow (y-2)Fe^{3+} + Mn^{2+}.$$

The excess of the Fe^{2+} was then titrated with 0.02 M $KMnO_4$.

III. RESULTS AND DISCUSSION

A. Composition, structural, and microstructural characterization at room temperature

Single-phase composition of the thin film and powder samples were confirmed by x-ray diffraction. EDX analyses of the powder compound are presented in Table I. The values have a small difference compared with those corresponding to the thin films in both types of analysis, EDX and RBS/ERDA measurements, shown in the same table. Moreover, the thin-film compositions show slightly different EDX values, depending on the analyzed region. The difference can result up to 10% when comparing the top surface layers and the nearest interface layers. Nevertheless, the compositional EDX values for thin films are in agreement with RBS-ERDA average data and also with those reported in Ref. 9. Despite the fact that the films were deposited from a sintered target with composition $La_{0.6}Ca_{0.4}MnO_3$, all analytical techniques reveal a composition near that of $La_{0.7}Ca_{0.3}MnO_3$. This suggests clearly that no congruent transfer of the La and Ca was achieved during PRCLA. A smaller amount of the lighter element in the film compared to the target can probably be explained by the higher degree of scattering of lighter elements. This produces a distribution of the light element in a large volume compared to the heavy element, yielding therefore films with reduced Ca content. This fact has also been observed for Li in $LiMn_2O_4$.[13]

The oxygen content analyzed by hot gas extraction in the powder samples gave a value of 2.90±0.05, which differs by a few percent to those obtained by EDX, since the last method is not as sensitive for light atoms. The average Mn valence for the powder compounds determined by redox titration was ~3.25+, with Mn^{3+} content of ~60%, and Mn^{4+} of ~35% (error in both measurement ~3%), and it is consistent with the compound stoichiometry.

Figure 1 shows the single-crystal x-ray diffraction data in the range of $20° < 2\theta < 80°$. The cubic $Pm\bar{3}m$, space

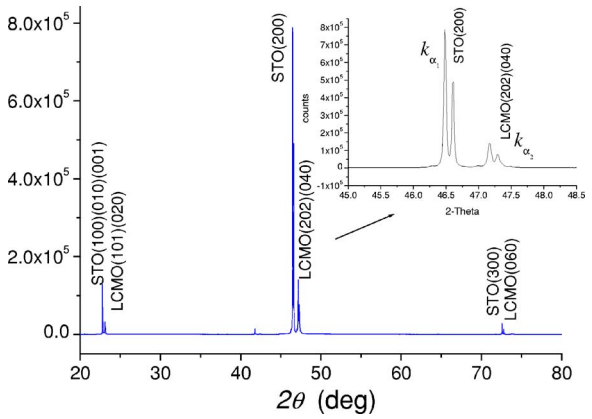

FIG. 1. (Color online) Single-crystal x-ray diffraction pattern of thin film and substrate.

grouping (S.G.) was used for indexing the $SrTiO_3$ substrate (Code: 01-089-4934), $a=0.3905$ nm, and the orthorhombic *Pnma* S.G. for the $La_{0.6}Ca_{0.4}MnO_{3-\delta}$ (LCMO) thin film, based on reference data.[14–16] The x-ray diffraction pattern of the powder sample and single crystal exhibit an orthorhombic distortion of the perovskite cell ($a \approx a_p\sqrt{2}$, $b \approx 2a_p$, $c \approx a_p\sqrt{2}$, $a_p \approx 0.4$ nm). Both powder materials and epitaxial films showed complicated electron diffraction patterns with twins, where two or more zone axis are overlapped. Single SAED patterns, as it is shown in Fig. 2, were occasionally found. For example, electron diffraction patterns taken on the powder compound corresponding to $[010]_o$, $[110]_o$, and $[101]_o$ zone axis, are shown in Figs. 2(a)–2(c), respectively. The indexation is based on an orthorhombic unit cell with cell parameters $a=0.548$ nm, $b=0.777$ nm, and $c=0.550$ nm. The extinction conditions imposed by the *Pnma* S.G. are not completely fulfilled in the diffraction patterns shown in Fig. 2, since the reflections $h00$ and $00l$ with $h,l=2n+1$ appear in the $[010]_o$ zone axis, $h00$ with $h=2n+1$ appear in the $[011]_o$ zone axis, and $0k0$ with $k=2n+1$ also appears in the $[101]_o$ zone axis. It was carefully checked that these additional reflections are not due to double diffraction, by performing tilting experiments along the ⟨100⟩, ⟨010⟩, and ⟨001⟩ axis. The studies by electron microscopy seem to indicate a breakdown of the orthorhombic symmetry, at least on the microdomain scale, by a small monoclinic distortion. To confirm this possibility, diffraction patterns with the structural model in *Pnma* and $P2_1/c$ space groups were simulated

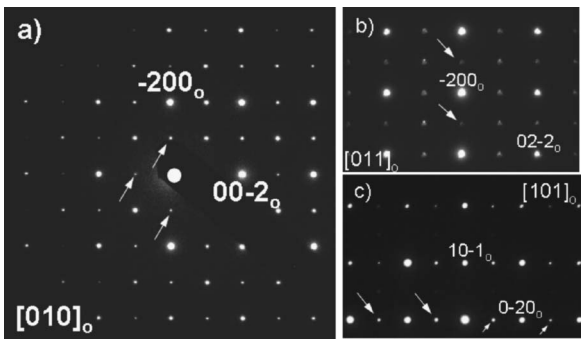

FIG. 2. Single zone axis (a) $[010]_o$, (b) $[011]_o$, and (c) $[101]_o$ electron diffraction patterns of LCMO powder samples.

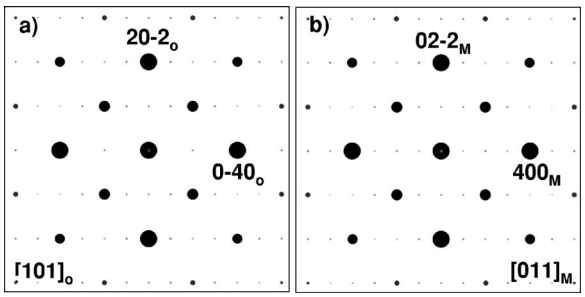

FIG. 3. (Color online) Theoretical simulation of (a) $[101]_o$ and (b) $[011]_o$ SAED patterns by JEMS.

by JEMS software.[17] Figure 3 shows the comparison of (a) $[101]_o$ zone axis in the *Pnma* S.G. with the unit cell describe above, and (b) $[011]_M$ zone axis in the $P2_1/c$ S.G., with $a=0.777$ nm, $b=0.550$ nm, $c=0.548$ nm, and $\beta=90.1°$. From these results, the $P2_1/c$ S.G. seems to be the best the structure of this compound.

TEM analysis of the thin film, prepared in cross-sectional geometry, presents similar features. A film of LCMO with approximately 210 nm thickness on a $SrTiO_3$ substrate is shown in Fig. 4(a). Figures 4(b) and 4(c) represent the experimental diffraction patterns of the substrate and thin film, respectively. Three different zone axis can be assigned in the electron diffraction pattern and they are shown in Fig. 4(c). They are indexed in the monoclinic structure with $P2_1/c$ S.G. The SAED pattern reveals the zone axis with the $\hat{\boldsymbol{a}}$ direction (long axis in the structure) in three space directions, giving apparently three different unit cells $\sim 2a_p \times a_p\sqrt{2} \times a_p\sqrt{2}$, $a_p\sqrt{2} \times 2\ a_p$ $x a_p\sqrt{2}$, and $a_p\sqrt{2} \times a_p\sqrt{2} \times 2a_p$. This is due to the twinning of the crystal, which is very often observed in perovskite materials with $a/\sqrt{2} \approx b \approx c$ parameters.[7] The HREM images in Figs. 5(a) and 5(c) confirm the presence of twins. Figure 5(b) shows the fast Fourier transform (FFT) corresponding to the HREM image of Fig. 5(a), where the long axis $\hat{\boldsymbol{a}}_{\boldsymbol{M}}$ can be observed in two directions, i.e., in the diffraction plane and perpendicular to the

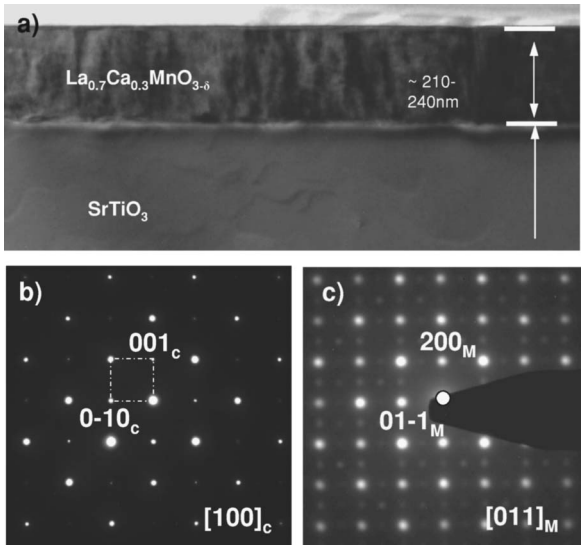

FIG. 4. (a) Cross-sectional TEM image of LCMO/STO and (b) [100] STO SAED pattern, (c) $[011]_M$ LCMO SAED pattern.

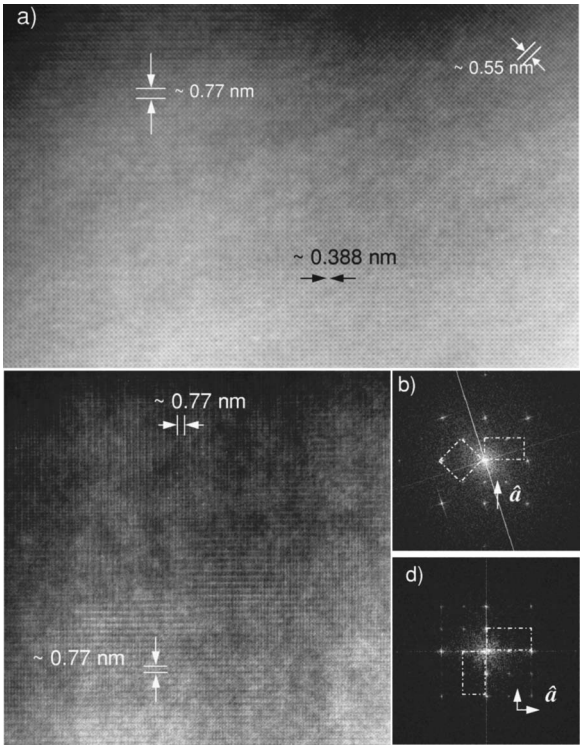

FIG. 5. (a) and (c) HREM images showing different twin domains in the thin film; (b) and (d) FFT from (a) and (c), respectively, with the two projected unit cells (overlapped) marked.

diffraction plane. Figure 5(c) exhibits twins with the $\hat{a}_M$ in the diffraction plane, which is confirmed by the corresponding FFT in Fig. 5(d).

Figure 6 presents the LCMO/$SrTiO_3$ interface analysis by TEM and reveals two different situations. The LCMO film exhibits an epitaxial growth with "cube-on-cube" on the $SrTiO_3$ substrate [see Fig. 6(a)]. Even though the lattice mismatch between LCMO and $SrTiO_3$ is very low (0.033%), some stress appears at the interface, illustrated in Fig. 6(a) with dark/white regions. To enhance the appearance of misfit dislocations at the interface, a Fourier filter of the HREM image (by Digital Micrograph) was applied, keeping the $\boldsymbol{g} = \langle 010 \rangle_p // \langle 0-11 \rangle_M$ direction in the diffraction pattern. The source of stress at the interfaces produced by the dislocations is observed in Fig. 6(b). Another region of the interface is shown in Fig. 6(c), which reveals a structural modulation in the direction $\boldsymbol{q} \approx 1/4[21-1]_M$. This is also confirmed by FFT. One possible explanation for this modulation can be obtained from the high-resolution image, where the structure seems to be formed by two repeating La–Mn–O layers followed by the two layers of La–Mn–Ca–Mn–O, which form a body-centered superstructure with the unit cell of $2a_p \times 4a_p$. The theoretical stoichiometry for this superstructure is $La_{3/4}Ca_{1/4}MnO_3$, which is different from the nominal composition but is in good agreement with the EDX analysis for the interface. The distribution of local stress is much more noticeable in this interface region due to the contrast of diagonal fringes, with tensile- and compressivelike stripes. It is quite probable that the local stress is released by the formation of the superstructure with the unit cell $2a_p \times 4a_p$. Regions of heavy stress have also been observed in LCMO thin

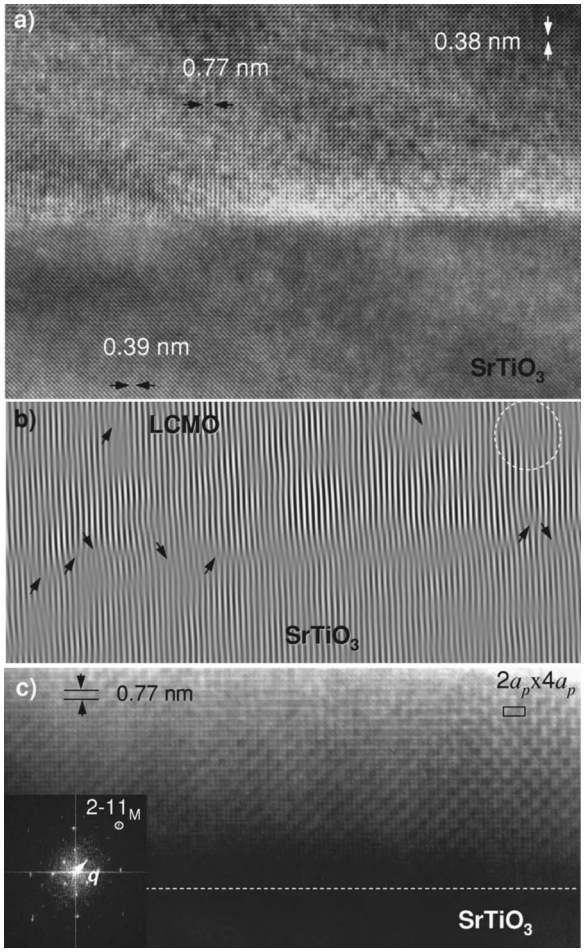

FIG. 6. (a) HREM image of the LCMO/STO interface; (b) Fourier filtered image of the interface (see the text for more details); and (c) HREM of the interface showing a structural modulation.

films grown on MgO(100) due to large mismatch (7.6%).[18] The superstructure described above has been observed as well in the thin films on MgO substrates, but it has not yet been reported for LCMO thin film on $SrTiO_3$ substrates. The nonuniform structure and composition (phase separation) may induce electronic inhomogeneities and therefore influence the transport properties, which is important for CMR applications.

B. High-temperature transport properties (350 K < *T* < 1200 K)

The resistivities of the polycrystalline LCMO compound and thin film show a semiconductor-like behavior between 350 K and 1200 K, and $d\boldsymbol{\rho}/dT < 0$ (see Fig. 7). Two different regimes are detected, the first up to ~500 K and the second above 500 K, where the $|d\boldsymbol{\rho}/dT|$ value is larger for the first region than the second one. Since a polycrystalline material contains significant contributions from grain boundaries to the resistivity, higher resistivity values are expected than for the thin films, as it is shown by the inset in Fig. 7. The analysis of the Seebeck coefficient in the same temperature range is more complex. Figure 8 shows the different behavior of the thermopower in LCMO thin films and LCMO polycrystalline samples. The measurement was done in the

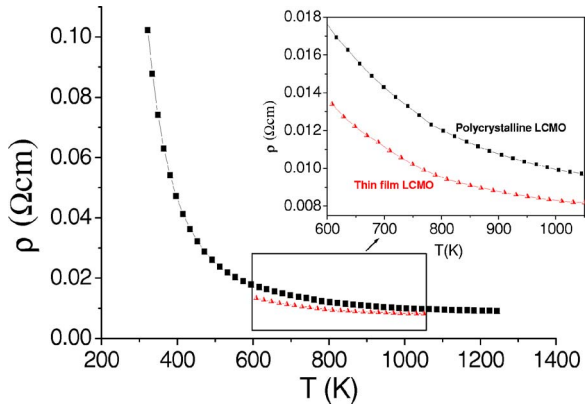

FIG. 7. (Color online) Resistivity vs temperature for the powder sample and LCMO/STO.

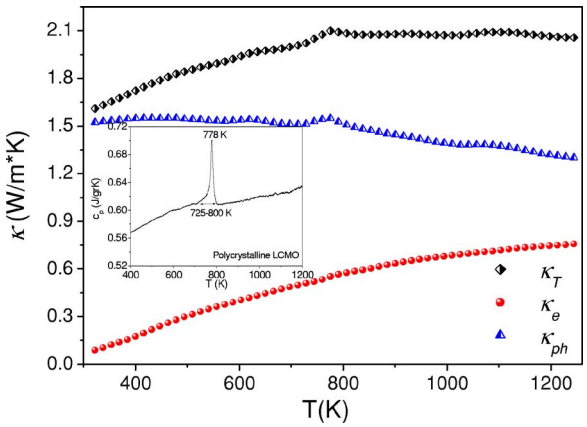

FIG. 9. (Color online) Thermal conductivity vs temperature for LCMO powder sample with specific heat vs temperature inset.

temperature range far from the metal-insulator transition ($T_{MI} \sim 150$ K) that was reported in Ref. 9. Therefore, no singularities, due the mentioned transition in the Seebeck values, are expected. For the polycrystalline compounds, the Seebeck coefficient is negative in the whole range of measurement, indicating the presence of electron-type charge carriers, and with values ranging from $S=-20$ μV/K to $S=-30$ μV/K. These values are in good agreement with those previously reported[19–21] and with the calculated high-temperature limit of the thermopower given by Heikes' formula for this compound.

The Seebeck coefficient of the thin film shows two sign changes, at 537 and 890 K, the first one from positive to negative values, and the second one from negative to positive values. This suggests that is possible to divide the temperature range into regions with different carrier contributions (see Fig. 8). In region **I** ($T<537$ K) with a Seebeck coefficient of $S>0$, the hole-like conduction type dominates; in region **II** (537 K$<T<$890 K), with a Seebeck coefficient of $S<0$, an electron conduction type is observed; while in region **III**, again with $S>0$, p-type conduction predominates. Taking into account that thin films have an average cationic composition of La/Ca/Mn$\approx$0.74/0.26/0.85, the Seebeck coefficient $S>0$ is in good agreement with the published data[22] up to 400 K. The polycrystalline compound has a slightly different cationic composition (La/Ca/Mn $\approx$0.63/0.36/0.95) compared to the thin film, with mixed Mn valence states: $Mn^{3+}/Mn^{4+}=3.25$, $Mn^{3+} \sim 35\%$, and $Mn^{4+} \sim 60\%$ experimentally obtained. The theoretically calculated Mn valence states for the thin film are $Mn^{3+} \approx 54\%$ and $Mn^{4+} \approx 31\%$. So, this difference in the amount of Mn^{3+} and Mn^{4+} can partially explain the different type of charge carrier and Seebeck behavior between thin-film and powder samples and is also related to the different oxygen content.[20–23] The distinctive microstructure found in the thin film (especially at the interface film/substrate) and the compositional inhomogeneities may also affect the Seebeck coefficient and charge carrier mobility. Both materials suffer a structural transition at $T \approx 750$ K, from "orthorhombic/monoclinic" to rhombohedral,[1] but it is in the thin film where the transition has larger influence than in polycrystalline powder. At this transition temperature, the Seebeck coefficient adopts a minimum value and starts to increase, taking positive values, i.e., $dS/dT>0$ for $T>750$ K. On the contrary, the Seebeck coefficients of polycrystalline samples show large negative values and $dS/dT<0$.

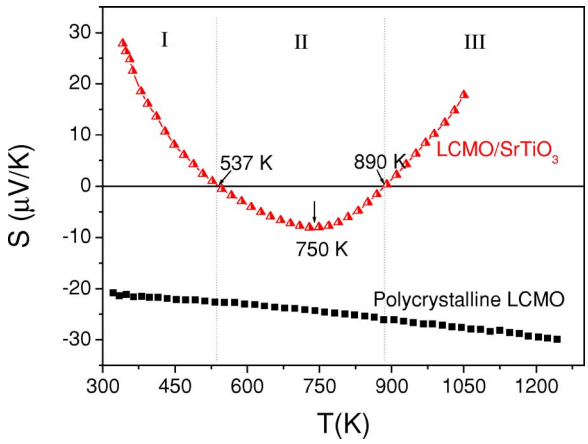

FIG. 8. (Color online) Seebeck coefficient as a function of temperature for the LCMO powder sample and LCMO/STO.

The thermal conductivity and specific heat, c_p, at high temperatures for LCMO polycrystalline samples were measured in order to get further insight into the transport properties. The results of the measurements are shown in Fig. 9. The total thermal conductivity, κ_t, increases with temperature up to 800 K, from $\kappa_t=1.5$ to 2.1 W/mK (typical values for oxide materials), and remains constant up to 1200 K. At around 770 K, κ_t reveals a peak that coincides with the position of a transition peak in the specific heat (see inset in Fig. 9) which has been attributed to a structural transition from orthorhombic $Pnma$ (or monoclinic $P2_1/c$) to rhombohedral structure $R\bar{3}c$.[1] The total thermal conductivity is composed of the phonon contribution κ_{ph} and the electronic contribution κ_e. The electronic component can be related to the electrical conductivity σ by the Wiedemann–Franz law: $\kappa_e = L_0 \sigma T$, where L_0 is the Lorentz number and T is absolute temperature. Figure 9 also includes these two components of thermal conductivity. The phonon conductivity stays approximately constant up to the structural transition temperature, where a small peak is observed. Above this temperature, a slight decrease can be observed. The phonon

conductivity is the predominant contribution to the total thermal conductivity, which is typical for oxides. The electronic thermal conductivity increases monotonically with temperature, but the values are low compared to the phonon thermal conductivity. The structural transition seems to have less influence on κ_e (the tendency of increasing values remains) for polycrystalline samples, while the lattice heat conduction, κ_{ph}, reflects the same event as the total thermal conductivity.

IV. CONCLUSIONS

In summary, the analysis of structural data shows the existence of a breakdown of the symmetry *Pnma* in favor of $P2_1/c$, in both types of materials, i.e., thin films and powder compound of LCMO. The structure can be described in terms of a distorted perovskite with unit cell parameters about $2a_p \times a_p\sqrt{2} \times a_p\sqrt{2}$. Thin films present an interface with low- and high-stress regions that are released by means of misfit dislocations. The modulation in the structure is produced by the new pile-up of atoms: La–Mn–O/La–Mn–Ca–Mn–O, which was found at the LCMO/$SrTiO_3$ interface and produces a supercell $2a_p \times 4a_p$. The phase separation is one way to adjust the compositional inhomogeneities and also to release the stress at the interface. This phenomenon produces different electronic densities or the so-called *electronic phase separation* that may influence the transport properties.[24]

The resistivities of both types of materials present semiconductorlike behavior, $d\boldsymbol{\rho}/dT < 0$, with two different regimes, since the resistivity changes the derivative values at $T \approx 500$ K from higher to smaller values. Seebeck coefficients as a function of temperature behave as the reported data[20,22] up to 400 K. Above this temperature, the powder compound follows the Heikes formula, while thin film differs from theoretical values. The behavior can be explained in terms of the structural transition and local inhomogeneities (which concerns local structural and compositional deviations). The value of mixed valence Mn^{3+}/Mn^{4+} for the thin film is in the "edge" of the majority electron/hole type charge carriers, and a small variation of oxygen content with temperature can influence this ratio and thus, the Seebeck coefficient. The structural transition also influences the thermal conductivity, especially in the phonon contribution.

ACKNOWLEDGMENTS

The authors would like to thank the Swiss Federal Office of Energy (BFE), Swiss National Science Foundation, PSI, and Empa for financial support, and Matthias Trottmann for technical assistance.

[1] P. Radaelli, M. Marezio, A. Hwang, S.-W. Cheong, and B. Battlog, Phys. Rev. B **54**, 8992 (1996).
[2] M. Roy, J. Mitchell, A. Ramirez, and P. Schiffer, J. Phys.: Condens. Matter **11**, 4843 (1999).
[3] C. Zener, Phys. Rev. **82**, 403 (1951).
[4] M. H. Aguirre, R. Ruiz-Bustos, and M. A. Alario-Franco, J. Mater. Chem. **13**, 1156 (2003).
[5] V. Moshnyaga, S. Klimm, E. Gommert, R. Tidecks, and S. Horn, J. Appl. Phys. **88**, 5305 (2000).
[6] E. Gommert, H. Cerva, J. Wecker, and K. Samwer, J. Appl. Phys. **85**, 5417 (1999).
[7] A. Weidenkaff, M. H. Aguirre, T. Lippert, U. Falke, and U. Bangert, Chimia **60**, 742 (2006).
[8] M. J. Montenegro, C. Clerc, T. Lippert, S. Müller, P. R. Willmott, A. Weidenkaff, and A. Wokaun, Appl. Surf. Sci. **208–209**, 45 (2003).
[9] S. Canulescu, T. Lippert, H. Crimmer, A. Wokaun, R. Robert, D. Logvinovich, A. Weidenkaff, and M. Döbeli, Appl. Surf. Sci. **252**, 4599 (2006).
[10] R. Robert, S. Romer, A. Reller, and A. Weidenkaff, Adv. Eng. Mater. **7**, 303 (2005).
[11] M. H. Aguirre, R. Robert, D. Logvinovich, and A. Weidenkaff, Inorg. Chem. **46**, 2744 (2007).
[12] E. Bloom, T. Kometany, and J. Mitchell, J. Inorg. Nucl. Chem. **40**, 403 (1978).
[13] Th. Dumont, T. Lippert, M. Döbeli, H. Grimmer, J. Ufheil, P. Novák, A. Wuersig, U. Vogt, and A. Wokaun, Appl. Surf. Sci. **252**, 4902 (2006).
[14] J. Blasco, J. Garcia, J. M. de Teresa, M. R. Ibarra, P. A. Algarabel, and C. Marquina, J. Phys.: Condens. Matter **8**, 7427 (1996).
[15] S. J. Hibble, S. P. Cooper, A. C. Hannon, I. D. Fawcett, and M. Greenblatt, J. Phys.: Condens. Matter **11**, 9221 (1999).
[16] P. M. Woodward, T. Vogt, D. E. Cox, A. Arulraj, C. N. R. Rao, P. Karen, and A. K. Cheethan, Chem. Mater. **10**, 3652 (1998).
[17] P. A. Stadelmann, Ultramicroscopy **21**, 131 (1987).
[18] V. Moshnyaga, L. Sudheendra, O. Lebedev, S. Köster, K. Gehrke, O. Shapoval, A. Belenchuk, A. Damaschke, G. van Tendeloo, and K. Samwer, Phys. Rev. Lett. **97**, 107205 (2006).
[19] T. Palstra, A. Ramirez, S. Cheong, B. Zegarski, P. Schiffer, and J. Zaanen, Phys. Rev. B **56**, 5104 (1997).
[20] R. Mahendiran, S. Tiwary, A. Raychaudhuri, T. Ramakrishnan, R. Mahesh, N. Rangavittal, and C. N. Rao, Phys. Rev. B **53**, 3348 (1996).
[21] W. Kobayashi, I. Terasaki, M. Mikami, R. Funahashi, T. Nomura, and T. Katsufuji, J. Appl. Phys. **95**, 6825 (2004).
[22] M. Hundley and J. Neumeier, Phys. Rev. B **55**, 11511 (1997).
[23] A. Maignan, V. Caignaert, D. Pelloquin, S. Hébert, V. Pralong, J. Hejtmanek, and D. Khomskii, Phys. Rev. B **74**, 165110 (2006).
[24] K. H. Ahn, T. Lookman, and A. R. Bishop, Nature **428**, 401 (2004).